CrossMark

JM PAPERS

Boundary zonal flows in rapidly rotating turbulent thermal convection

Xuan Zhang[1],†, **Robert E. Ecke**[2,3] **and Olga Shishkina**[1],†

[1]Max Planck Institute for Dynamics and Self-Organization, Am Fassberg 17, 37077 Göttingen, Germany

[2]Center for Nonlinear Studies, Los Alamos National Laboratory, Los Alamos, NM 87545, USA

[3]Department of Physics, University of Washington, Seattle, WA 98195, USA

Recently, in Zhang *et al.* (*Phys. Rev. Lett.*, vol. 124, 2020, 084505), it was found that, in rapidly rotating turbulent Rayleigh–Bénard convection in slender cylindrical containers (with diameter-to-height aspect ratio $\Gamma = 1/2$) filled with a small-Prandtl-number fluid ($Pr \approx 0.8$), the large-scale circulation is suppressed and a boundary zonal flow (BZF) develops near the sidewall, characterized by a bimodal probability density function of the temperature, cyclonic fluid motion and anticyclonic drift of the flow pattern (with respect to the rotating frame). This BZF carries a disproportionate amount ($>60\%$) of the total heat transport for $Pr < 1$, but decreases rather abruptly for larger Pr to approximately 35 %. In this work, we show that the BZF is robust and appears in rapidly rotating turbulent Rayleigh–Bénard convection in containers of different Γ and over a broad range of Pr and Ra. Direct numerical simulations for Prandtl number $0.1 \leq Pr \leq 12.3$, Rayleigh number $10^7 \leq Ra \leq 5 \times 10^9$, inverse Ekman number $10^5 \leq 1/Ek \leq 10^7$ and $\Gamma = 1/3$, 1/2, 3/4, 1 and 2 show that the BZF width δ_0 scales with the Rayleigh number Ra and Ekman number Ek as $\delta_0/H \sim \Gamma^0 Pr^{\{-1/4,0\}} Ra^{1/4} Ek^{2/3}$ ($\{Pr < 1, Pr > 1\}$) and with the drift frequency scales as $\omega/\Omega \sim \Gamma^0 Pr^{-4/3} Ra\, Ek^{5/3}$, where H is the cell height and Ω the angular rotation rate. The mode number of the BZF is 1 for $\Gamma \lesssim 1$ and 2Γ for $\Gamma = \{1, 2\}$ independent of Ra and Pr. The BZF is quite reminiscent of wall mode states in rotating convection.

Key words: Bénard convection, rotating flows, rotating turbulence

1. Introduction

Turbulent convection driven by buoyancy and subject to background rotation is a phenomenon of great relevance in many physical disciplines, especially in geo- and

† Email addresses for correspondence: xuan.zhang@ds.mpg.de, Olga.Shishkina@ds.mpg.de

915 A62-1

astrophysics and also in engineering applications. In a model system of Rayleigh–Bénard convection (RBC) (Bodenschatz, Pesch & Ahlers 2000; Ahlers, Grossmann & Lohse 2009; Lohse & Xia 2010), a fluid is confined in a container where the bottom is heated, the top is cooled and the vertical walls are adiabatic. The temperature inhomogeneity leads to a fluid density variation, which, in the presence of gravity, produces convective fluid motion. When the system rotates with respect to the vertical axis, significant modification of the flow occurs owing to the rotational influence, including the suppression of the onset of convection (Nakagawa & Frenzen 1955; Chandrasekhar 1961), the enhancement or suppression of turbulent heat transport over different ranges of Rayleigh number Ra and Prandtl number Pr (Rossby 1969; Pfotenhauer, Niemela & Donnelly 1987; Zhong, Ecke & Steinberg 1993; Julien *et al.* 1996; Liu & Ecke 1997), the transformation of thermal plumes into thermal vortices with a rich variety of local structure dynamics (Boubnov & Golitsyn 1986, 1990; Hart, Kittelman & Ohlsen 2002; Vorobieff & Ecke 2002) and the emergence of robust wall modes before the onset of the bulk mode (Buell & Catton 1983; Pfotenhauer *et al.* 1987; Zhong, Ecke & Steinberg 1991; Ecke, Zhong & Knobloch 1992; Goldstein *et al.* 1993; Herrmann & Busse 1993; Kuo & Cross 1993).

The dimensionless control parameters in rotating RBC are the Rayleigh number $Ra \equiv \alpha g \Delta H^3/(\kappa \nu)$, the Prandtl number $Pr \equiv \nu/\kappa$, the Ekman number $Ek \equiv \nu/(2\Omega H^2)$ and the diameter-to-height aspect ratio of the container, $\Gamma \equiv D/H$. Here α denotes the isobaric thermal expansion coefficient, ν the kinematic viscosity, κ the thermal diffusivity of the fluid, g the acceleration due to gravity, Ω the angular rotation rate, $\Delta \equiv T_+ - T_-$ the difference between the temperatures at the bottom (T_+) and top (T_-) plates, H the distance between the isothermal plates (the cylinder height) and $D \equiv 2R$ the cylinder diameter. The Rossby number $Ro \equiv \sqrt{\alpha g \Delta H}/(2\Omega H) = \sqrt{Ra/Pr}\, Ek$ is another important non-dimensional parameter that provides a measure of the balance between buoyancy and rotation and is independent of dissipation coefficients.

The important global response parameter in thermal convection is the averaged total heat transport between the bottom and top plates, described by the Nusselt number, $Nu \equiv (\langle u_z T \rangle_z - \kappa \partial_z \langle T \rangle_z)/(\kappa \Delta/H)$. Here, T denotes the temperature, $\boldsymbol{u}$ is the velocity field with component u_z in the vertical direction, and $\langle \cdot \rangle_z$ denotes the average in time and over a horizontal cross-section at height z from the bottom.

Rotation has various effects on the structure of the convective flow and on the global heat transport in the system. Rotation inhibits convection and causes an increase of the critical $Ra_c \sim Ek^{-4/3}$ at which the quiescent fluid layer becomes unstable throughout the layer (Nakagawa & Frenzen 1955; Chandrasekhar 1961; Rossby 1969; Lucas, Pfotenhauer & Donnelly 1983; Zhong *et al.* 1993). In finite containers and at sufficiently large rotation rates, however, a different instability occurs at lower $Ra_w \sim Ek^{-1}$ in the form of anticyclonically drifting wall modes (Buell & Catton 1983; Pfotenhauer *et al.* 1987; Zhong *et al.* 1991; Ecke *et al.* 1992; Goldstein *et al.* 1993; Herrmann & Busse 1993; Kuo & Cross 1993; Ning & Ecke 1993; Zhong *et al.* 1993; Goldstein *et al.* 1994; Liu & Ecke 1997, 1999; Zhang & Liao 2009; Favier & Knobloch 2020). The relative contribution of the wall modes to the total heat transport depends on Γ (Rossby 1969; Pfotenhauer *et al.* 1987; Ning & Ecke 1993; Zhong *et al.* 1993; Liu & Ecke 1999) with decreasing contribution – roughly as the perimeter-to-area ratio – with increasing Γ.

There are several regions of bulk rotating convection where rotation plays an important role, namely a rotation-affected regime and a rotation-dominated regime. In the former, where $Ro \lesssim 1$, heat transport varies as a power law in Ra, i.e. $Nu = A(Ek)Ra^{0.3}$, and can be enhanced or weakly suppressed by rotation relative to the heat transport without rotation (Rossby 1969; Zhong *et al.* 1991; Julien *et al.* 1996; Liu & Ecke 1997; King *et al.* 2009;

Liu & Ecke 2009; Zhong *et al.* 2009) depending on the range of *Ra* and *Pr*. In the latter case, in which $Ro \ll 1$, heat transport changes much more rapidly with *Ra* in what is known as the geostrophic regime of rotating convection (Sakai 1997; Grooms *et al.* 2010; Julien *et al.* 2012; Ecke & Niemela 2014; Stellmach *et al.* 2014; Cheng *et al.* 2020).

Despite considerable previous work, the spatial distribution of flow and heat transport in confined geometries has not been well studied for high *Ra* and low *Ro* when one is significantly above the onset of bulk convection but still highly affected by rotation. Recently, Zhang *et al.* (2020) demonstrated in direct numerical simulations (DNS) and experiments that a boundary zonal flow (BZF) develops near the vertical wall of a slender cylindrical container ($\Gamma = 1/2$) in rapidly rotating turbulent RBC for $Pr = 0.8$ (pressurized gas SF_6) and over broad ranges of *Ra* ($Ra = 10^9$ in DNS and for $10^{11} \lesssim Ra \lesssim 10^{14}$ in experiments) and *Ek* ($10^{-6} \lesssim Ek \lesssim 10^{-5}$ in the DNS and for $3 \times 10^{-8} \lesssim Ek \lesssim 3 \times 10^{-6}$ in experiments). The BZF becomes the dominant mean flow structure in the cell for $Ro \lesssim 1$, at which the large-scale mean circulation (termed the large-scale circulation; LSC) vanishes (Vorobieff & Ecke 2002; Kunnen *et al.* 2008; Weiss & Ahlers 2011*a*,*b*). Further, it contributes a disproportionately large fraction of the total heat transport.

Another group (de Wit *et al.* 2020) also showed the existence of the BZF and its strong influence on heat transport using DNS for $Pr = 5$ (water) and $\Gamma = 1/5$ for $Ek = 10^{-7}$ in the range $5 \times 10^{10} \lesssim Ra \lesssim 5 \times 10^{11}$. Thus, the BZF has been observed in different fluids, in cells of different aspect ratios and over a wide range of parameter values. Given the strongly enhanced heat transport in the BZF region (de Wit *et al.* 2020; Zhang *et al.* 2020), it is important to explore the BZF in detail. Here we investigate the robustness of the BZF with respect to *Pr* and to Γ in the geostrophic regime; we do not address here the transition from the low rotation state to the BZF.

Recently, Favier & Knobloch (2020) demonstrated for $Ek = 10^{-6}$ through DNS that the linear wall modes of rotating convection (Buell & Catton 1983; Zhong *et al.* 1991; Ecke *et al.* 1992; Goldstein *et al.* 1993; Herrmann & Busse 1993; Kuo & Cross 1993; Ning & Ecke 1993; Zhong *et al.* 1993; Liu & Ecke 1997, 1999; Sánchez-Álvarez *et al.* 2005; Horn & Schmid 2017; Aurnou *et al.* 2018) evolve with increasing *Ra* and appear to be robust with respect to the emergence of bulk convection even with well-developed turbulence. They suggested that the BZF may be the nonlinear evolution of wall modes, an idea that we address briefly but that requires significantly more analysis and comparison than can be included here.

In the present work, a series of DNS is carried out to study the robustness and the scaling properties of the BZF with respect to Rayleigh number *Ra*, Ekman number *Ek*, Prandtl number *Pr* and cell aspect ratio Γ. We explore the extended scalings of the characteristics of the BZF, including the width of the BZF, the drift frequency of the BZF and the heat transport within the BZF in terms of these non-dimensional parameters. We first present our numerical methods, then discuss the results of our calculations and conclude with our main findings.

2. Numerical method

We present results of DNS of rotating RBC in a cylindrical cell obtained using the GOLDFISH code (Shishkina *et al.* 2015; Kooij *et al.* 2018) for *Ra* up to 5×10^9 and *Ek* down to 10^{-7}. In the DNS, the Oberbeck–Boussinesq approximation is assumed as in Horn & Shishkina (2014). Centrifugal force effects are neglected since the Froude number in experiments is typically small (see Zhong *et al.* 2009; Horn & Shishkina 2015).

The governing equations based on the Oberbeck–Boussinesq approximation are

$$\nabla \cdot \boldsymbol{u} = 0, \tag{2.1}$$

$$\partial_t \boldsymbol{u} + (\boldsymbol{u} \cdot \nabla)\boldsymbol{u} = -\frac{1}{\rho}\nabla p + \nu\nabla^2 \boldsymbol{u} - 2\boldsymbol{\Omega} \times \boldsymbol{u} + \alpha(T - T_0)g\boldsymbol{e}_z, \tag{2.2}$$

$$\partial_t T + (\boldsymbol{u} \cdot \nabla)T = \kappa\nabla^2 T. \tag{2.3}$$

Here, $\boldsymbol{u} = (u_r, u_\phi, u_z)$ is the velocity with radial, azimuthal and vertical coordinates, respectively, ρ is the density, p is the reduced pressure, $\boldsymbol{\Omega} = \Omega\boldsymbol{e}_z$ is the angular rotation-rate vector, T is the temperature with $T_0 = (T_+ + T_-)/2$, and $\boldsymbol{e}_z$ is the unit vector in the vertical direction. The applied boundary conditions are no slip for the velocity on all surfaces, constant temperature for the top and bottom plates and adiabatic for the sidewall. To non-dimensionalize the governing equations, we use $\Delta = T_+ - T_-$ as the temperature scale, the cylinder height H as the length scale and the free-fall velocity $\sqrt{\alpha g \Delta H}$ as the velocity scale (the corresponding time scale is $\tau_{ff} = \sqrt{H/(\alpha g \Delta)}$).

To evaluate the grid requirements for the simulations, we consider the thermal and velocity boundary layers (BLs) near solid boundaries. The thickness of the BLs near the heated and cooled plates are calculated as

$$\delta_{th} = H/(2Nu). \tag{2.4}$$

This is the standard way to define the thermal BL thickness under the assumption of pure conductive heat transport within this layer (cf. Ahlers *et al.* 2009). The viscous BL thicknesses near the plates (δ_u) and near the sidewall (δ^{sw}) are defined as the distances from the corresponding walls to the location where the maxima of, respectively, $\sqrt{\langle u_r^2 \rangle_{t,\phi,r} + \langle u_\phi^2 \rangle_{t,\phi,r}}$ (z) and $\sqrt{\langle u_\phi^2 \rangle_{t,\phi,z} + \langle u_z^2 \rangle_{t,\phi,z}}$ (r) are obtained. The velocity components are all averaged in time and over the surface parallel to the corresponding wall. The same criterion was used previously in studies of the sidewall layers in rotating convection (see Kunnen *et al.* 2011).

The computational grids are set to be sufficiently fine to resolve the mean Kolmogorov microscales (Shishkina *et al.* 2010) in the bulk and within the BLs (see table 2 in the Appendix). Grid nodes are clustered near the walls to resolve thermal and velocity BLs, resulting in grids that are non-equidistant in both the radial and vertical directions. As rotation increases, the viscous BL gets thinner (Kunnen *et al.* 2008; Stevens, Verzicco & Lohse 2010; Horn & Shishkina 2015) so more points are required near boundaries: we take at least seven points within each BL. The details of all simulated parameters and the corresponding grid resolution are listed in table 2 along with a benchmark comparison between Nu data from these simulations and from experimental data in compressed gases with similar Pr from Wedi *et al.* (2021); the agreement is excellent. To explore the robustness of the BZF with respect to Ra, Pr and Γ, we conducted simulations in three groups, i.e. in every group we vary only one parameter while keeping the others fixed. The specific parameter ranges are shown in table 1 (also included in several figures with $Ra = 10^9$ and $Pr = 0.8$ are data in the range $0.5 \leq 1/Ro \leq 5$ from Zhang *et al.* (2020); the calculation details for those values are included in the Appendix).

3. Results

3.1. *Boundary zonal flow structure*

Our goal here is to explore the robustness of the BZF with respect to variations of control parameters. We follow closely the approach and characterization presented in

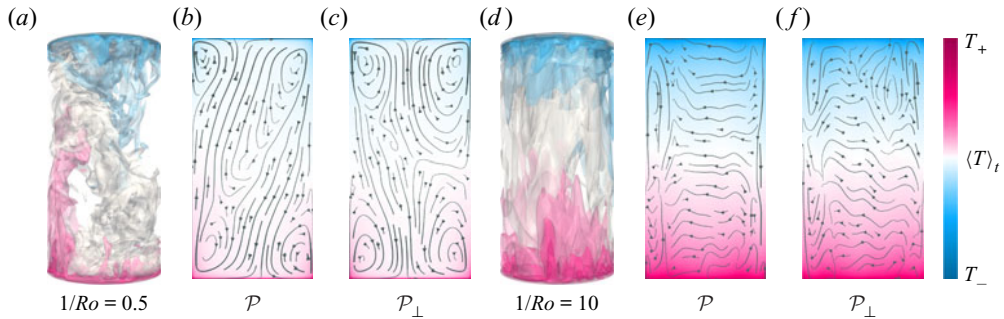| Γ	Pr	Ra (10^7)	$1/Ro$	Ek (10^{-6})
1/2	0.8	5–500	10	1.3–13
1/2	0.1–12.3	10	10	3.2–35
1/3–2	0.8	10	10	8.9
1/2	0.8	100	5.6–33.3	0.85–5.1

Table 1. Ranges of Γ, Ra, Pr, Ro^{-1} and Ek. For details, see the Appendix.

Figure 1. Isosurfaces of instantaneous temperature T (a) and time-averaged flow fields (b,c), visualized by streamlines (arrows) and temperature (colours), for $Ra = 10^9$ and $1/Ro = 10$, in vertical orthogonal planes $\mathcal{P}$ (b,e) and $\mathcal{P}_\perp$ (c,f). In the case of weak rotation (a–c), $\mathcal{P}$ is the plane of the LSC (b). Averaging in (b,c) is conducted over 1000 free-fall time units. For strong rotation (e,f), mean radial and axial velocity magnitudes are approximately 10-fold smaller than those for weak rotation (b,c).

Zhang *et al.* (2020) but focus on the geostrophic regime where the BZF is well developed. After presenting our main results, we consider the BZF with respect to wall mode structures. We begin with the influence of rotation on the overall temperature and velocity fields in the cell. In figure 1, for particular cases of $1/Ro = 0.5$ (weak rotation) and $1/Ro = 10$ (fast rotation), three-dimensional instantaneous temperature distributions (figure 1a,d) and two-dimensional vertical cross-sections (figure 1b,c,e,f) of the time-averaged flow fields are shown. The two-dimensional views are taken in a plane $\mathcal{P}$ (figure 1b,e), which in the case of a weak rotation is the LSC plane, and additionally in a plane $\mathcal{P}_\perp$ that is perpendicular to $\mathcal{P}$ (figure 1c,f). For slow rotation, an LSC spanning the entire cell with two secondary corner rolls is observed in $\mathcal{P}$ whereas a four-roll structure is seen in $\mathcal{P}_\perp$, typical of classical RBC at large Ra and for $\Gamma \sim 1$ (see e.g. Shishkina, Wagner & Horn 2014; Zwirner *et al.* 2020). Near the plates, the LSC and the secondary corner flows move the fluid towards the sidewall (figure 1b) so the Coriolis acceleration ($-2\Omega e_z \times u$) induces anticyclonic fluid motion close to the plates.

In the central part of the cell, at $z = H/2$, the radial component of the mean velocity, $\langle u_r \rangle_t$, always points towards the cell centre (figure 1a,b). Therefore, Coriolis acceleration results in cyclonic fluid motion in the central part of the cell, as is also observed in the time-averaged azimuthal velocity field u_ϕ in figure 2(a). Cases at higher rotation rates are shown in figures 1(d–f) and 2 (see also Kunnen *et al.* 2011). For both small and large rotation rates, the presence of viscous BLs near the plates implies anticyclonic motion of the fluid there. For strong rotation, the subject of this paper, with high and constant angular velocity Ω, the fluid velocity becomes more uniform along e_z owing
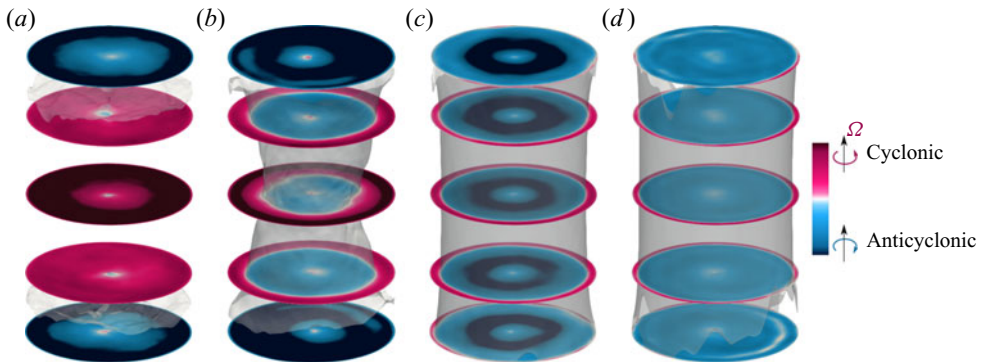
Figure 2. Time-averaged fields $\langle u_\phi \rangle_t$ for $Pr = 0.8$, $\Gamma = 1/2$, $Ra = 10^9$ and (a) $1/Ro = 0.5$, (b) $1/Ro = 2$, (c) $1/Ro = 10$ and (d) $1/Ro = 20$.

to the Taylor–Proudman constraint with larger components of lateral velocity compared to the vertical component as in figure 1(e, f). Thus, anticyclonic fluid motion not only is present in the vicinity of the plates, but also involves more and more fluid volume with increasing Ro^{-1}. With increasing rotation rate, anticyclonic motion grows from the plates towards the cell centre whereas cyclonic motion at $z = H/2$ remains near the sidewall and becomes increasingly more localized there (figure 2c,d).

As introduced in Zhang *et al.* (2020), the BZF in rapidly rotating turbulent convection is characterized by an anticyclonic bulk flow, cyclonic vortices clustering near the sidewall and anticyclonic drift of thermal plumes (see figures 3a,b and 4). These structures are associated with the bimodal temperature probability density functions (p.d.f.s) obtained in the measurements and DNS near the sidewall (Zhang *et al.* 2020; Wedi *et al.* 2021). The radial location r_0 where the mean fluid motion at $z/H = 1/2$ changes from anticyclonic to cyclonic as indicated by the solid line in figure 3 (see also inset of figure 6a below) is used to describe the width of the BZF $\delta_0 = R - r_0$. As one might expect, vertical coherence of the BZF is enhanced by strong rotation. In figure 4, time–angle plots of the temperature at three different heights show that the drift frequency $\omega = 2\pi R(\mathrm{d}\phi(r_{u_\phi^{max}})/\mathrm{d}t)/(2\pi R/m) = m\,\mathrm{d}\phi(r_{u_\phi^{max}})/\mathrm{d}t$ is quite constant along z without significant phase differences, i.e. the BZF maintains good vertical coherence. Here, the mode number m equals 1 and $\mathrm{d}\phi(r_{u_\phi^{max}})/\mathrm{d}t$ denotes the angular velocity of the temperature drift at $r = r_{u_\phi^{max}}$, where the maximum of the time-averaged azimuthal velocity is obtained. In the lower half of the cell, for $z = H/4$, warm plumes dominate, so the warm regions (pink stripes) are wider, whereas in the upper half of the cell, for $z = 3H/4$, cold plumes dominate, resulting in wider cooler regions (blue stripes). Similarly, figures 2(c,d) and 5(a,d) show that the zonal flow develops away from the top and bottom plates and extends vertically throughout the bulk. Figure 5 illustrates that, owing to the drift, time-averaged fields in the vertical plane average to zero and do not capture important features of the flow motion, in particular, the u_z field. The averaged u_z^2, however, does retain important information about the locations of the Stewartson '1/3' and '1/4' layers (dashed lines) and the BZF (solid line).

3.2. *Contribution to heat transport*

An important and unexpected property of the BZF in rotating RBC is its disproportionately large contribution to the heat transport in the system. Figures 3(a) and 6 show that the
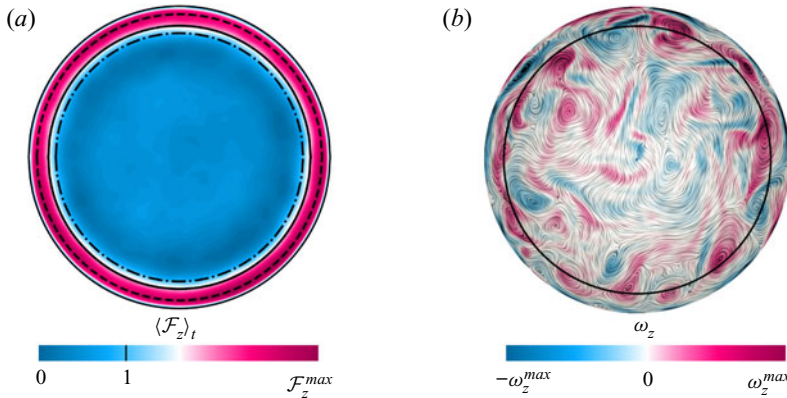
Figure 3. For $Ra = 10^9$, $1/Ro = 10$, $Pr = 0.8$, $\Gamma = 1/2$ and $z = H/2$: (a,b) horizontal cross-sections of (a) time-averaged vertical heat flux $\langle \mathcal{F}_z \rangle_t$ and (b) instantaneous vertical component of vorticity ω_z (negative values correspond to anticyclonic fluid motion), together with two-dimensional streamlines. The solid line indicates the radial position r_0 that defines the BZF by the condition $\langle u_\phi(r_0, z = H/2) \rangle_t = 0$. In (a), the dash-dotted line (inner circle) and the dashed line (outer circle) are, respectively, the radial locations of $\langle \mathcal{F}_z \rangle_t = 1$ (global averaged heat flux) and u_ϕ^{max}, the maximum of the time-averaged azimuthal velocity.
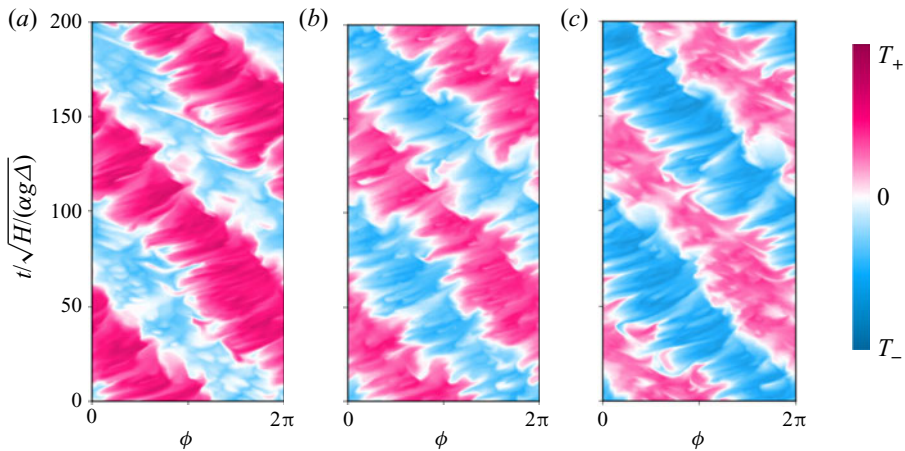
Figure 4. For $Pr = 0.8$, $\Gamma = 1/2$, $Ra = 10^9$, $1/Ro = 20$ and $r = R$: time evolution of temperature distribution (space–time plot of temperature) at height (a) $z = H/4$, (b) $z = H/2$ and (c) $z = 3H/4$.

averaged heat flux inside the BZF is much stronger than in the region outside the BZF. To be clear about the averaging, we define

$$\mathcal{F}_i(r, \phi, z) \equiv (u_i T - \kappa \partial_i T)/(\kappa \Delta/H), \quad i = r, \phi, z, \tag{3.1}$$

$$\langle Nu(r, t) \rangle_\phi \equiv (2\pi)^{-1} \int_0^{2\pi} \mathcal{F}_z(r, \phi, z = H/2) \, d\phi, \tag{3.2}$$

$$\langle Nu(t) \rangle_V \equiv (\pi R^2 H)^{-1} \int_0^{2\pi} \int_0^R \int_0^H \mathcal{F}_z(r, \phi, z) r \, dr \, d\phi \, dz, \tag{3.3}$$

$$\langle Nu(t) \rangle_{BZF} \equiv (\pi(R^2 - r_0^2))^{-1} \int_0^{2\pi} \int_{r_0}^R \mathcal{F}_z(r, \phi, z = H/2) r \, dr \, d\phi, \tag{3.4}$$

915 A62-7

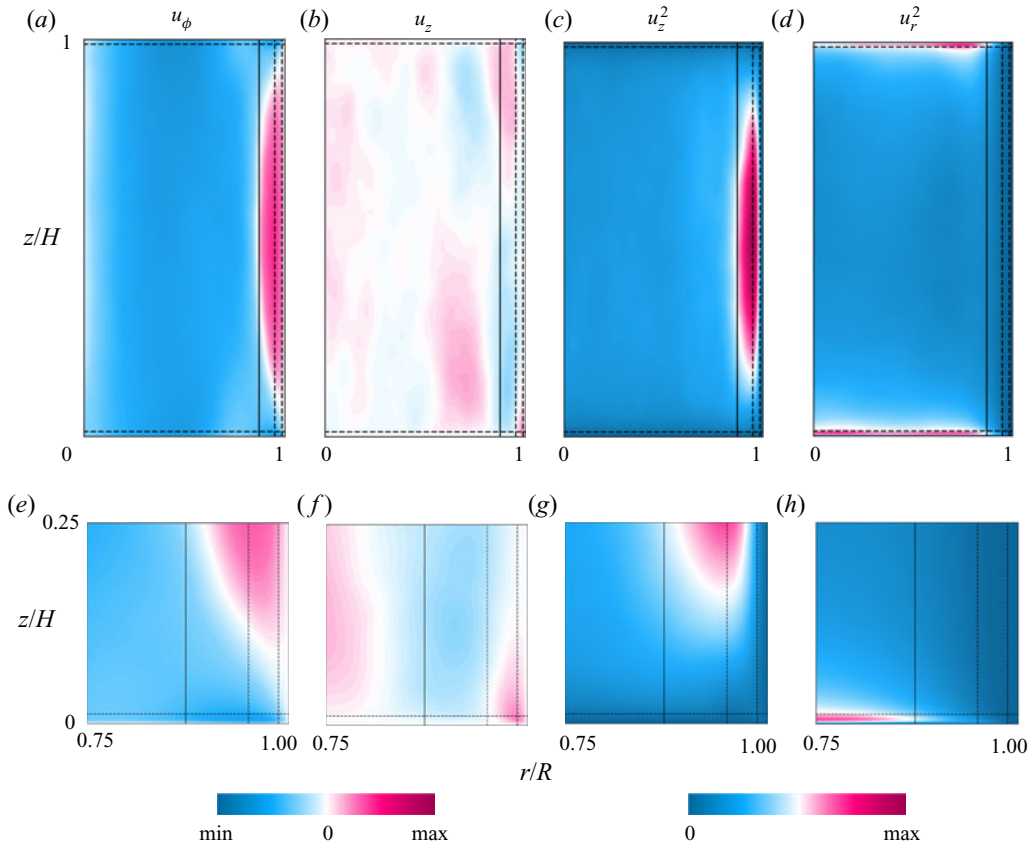Figure 5. Time-averaged flow fields in a vertical plane, for $Ra = 10^9$, $1/Ro = 10$, $Pr = 0.8$ and $\Gamma = 1/2$. The ranges of variables are, respectively: (a,b,e,f) from -0.17 to 0.17; and (c,d,g,h) from 0 to 0.0289.

$$R_f \equiv \langle Nu \rangle_{BZF,t} / \langle Nu \rangle_{V,t}, \tag{3.5}$$

$$R_h \equiv (\langle Nu \rangle_{BZF,t} \, \pi(R^2 - r_0^2)) / (\langle Nu \rangle_{V,t} \, \pi R^2) = \frac{R^2 - r_0^2}{R^2} \langle Nu \rangle_{BZF,t} / \langle Nu \rangle_{V,t}, \tag{3.6}$$

where $r_0 = R - \delta_0$. The quantity R_f is the ratio of the mean vertical heat flux within the BZF to the vertical heat flux averaged over the whole cell. The quantity R_h reflects the portion of the heat transported through the BZF compared to the total transported heat. Especially, in figure 6(a), the time- and ϕ-averaged radial profile at the mid-height for $Ra = 10^9$, $Pr = 0.8$ and $\Gamma = 1/2$ shows a significant peak of heat transport inside the BZF, and the peak amplitude increases dramatically as rotation becomes stronger. Thus, although the width of the BZF shrinks with increasing rotation, thereby reducing the effective area of the BZF with respect to the whole domain, as shown in figure 6(b), the increasing magnitude of the peak makes the heat transport carried by the BZF quite significant. Note that the annular BZF region of width δ_0 is smaller than the positive contribution to the heat transport, as shown in the inset of figure 6(a).

Figure 6(c) reveals that the enhancement of the local heat transfer within the BZF increases more rapidly when rotation is very strong ($1/Ro \gtrsim 10$). As a result of these properties, the heat transport carried by the BZF for these parameter values is always more than 60 % of the total heat transport at fast rotation (see figure 6d). Note, however, that the

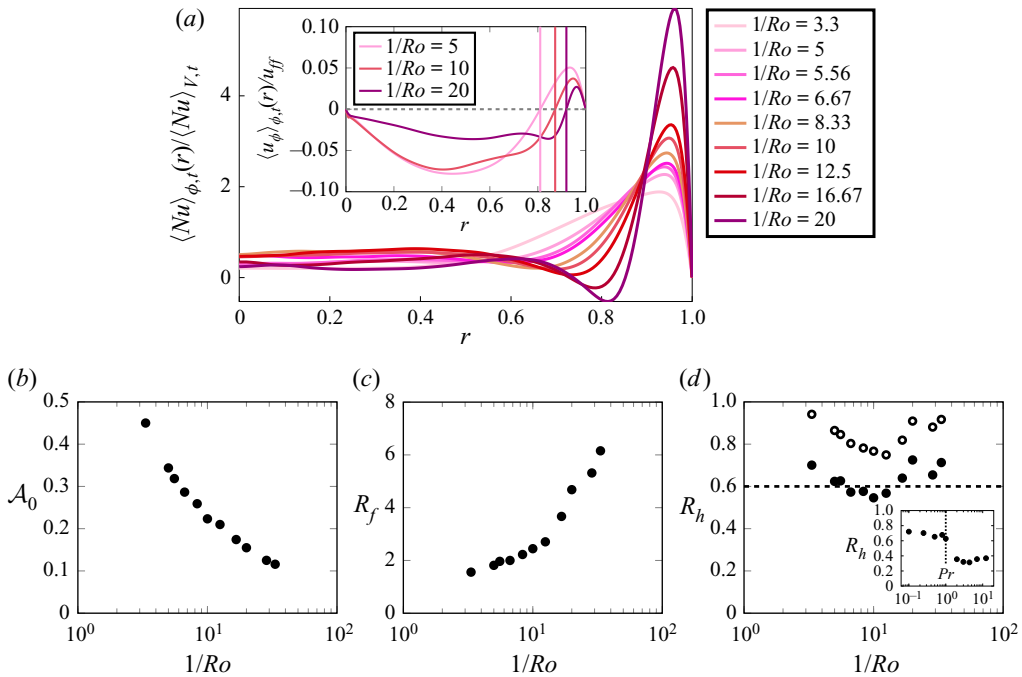**915** A62-8

Figure 6. (*a*) Radial profiles of normalized time- and ϕ-averaged heat flux $\langle Nu \rangle_{\phi,t}(r)/\langle Nu \rangle_{V,t}$ at $z = H/2$, for different rotation rates. The inset shows the radial profiles of time- and ϕ-averaged u_ϕ, where solid lines pass through $\langle u_\phi \rangle_{\phi,t} = 0$ (radial location corresponds to r_0). (*b*) Ratio of BZF area to the total area at $z = H/2$, i.e. $\mathcal{A}_0 = (R^2 - r_0^2)/R^2$. (*c*) Ratio of mean vertical heat flux inside the BZF to mean global heat flux, i.e. R_f (3.5). (*d*) Ratio of heat transported inside the BZF (solid circles) or in an extended zone $R - 2\delta_0 < r < R$ (open circles) to total transported heat, i.e. R_h (R_h^*) (3.6). For all panels $Ra = 10^9$, $Pr = 0.8$ and $\Gamma = 1/2$.

effect of the BZF on the heat transport extends over a wider range $r < r_0$; over some range, *Nu* is actually negative (see figure 6*a*), implying an anticorrelation of vertical velocity and buoyancy, i.e. warm fluid going down or cooler fluid moving up. If we modify the annular averaging to take into account the decreased *Nu* region as well as the inner structure of the BZF, i.e. we average over the extended region $R - 2\delta_0 \le r \le R$, we get the ratio R_h^*, which is also shown in figure 6(*d*) (open symbols) where one sees an even larger fractional contribution.

We also consider the dependence of the heat transport ratio R_h as a function of *Pr* (see inset of figure 6*d*). Interestingly, for $Pr < 1$ we find $0.6 < R_h < 0.7$, whereas for $Pr > 1$ we have $0.3 < R_h < 0.4$, with a quite sharp transition for $Pr \approx 1$. The origin of this rather sharp change emphasizes the important role that *Pr* plays, perhaps through the competition between thermal and viscous BLs. Finally, comparing our computation of the total *Nu* with increasing rotation with that of Wedi *et al.* (2021) (see figure 13 in the Appendix), we conclude, given the close agreement, that the contribution of the BZF affects both measures of *Nu* substantially and needs to be taken into account when considering the scaling of geostrophic heat transport in experiments and also in DNS with no-slip sidewall boundary conditions (see also de Wit *et al.* 2020).

3.3. *Dependence on Ra, Pr and Γ*

We first discuss the qualitative robustness of the BZF with respect to *Ra*, *Pr* and Γ before we consider its quantitative spatial and temporal properties. We demonstrate the character
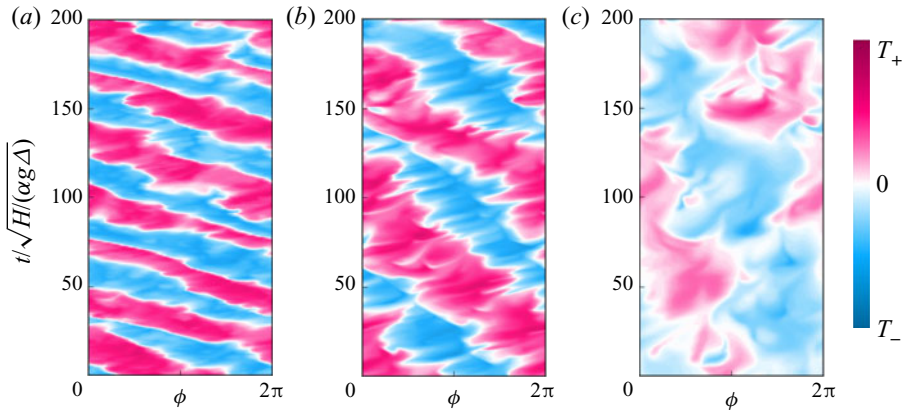
Figure 7. Space–time plots of temperature T at the sidewall, $r = R$, and at half-height, $z = H/2$, for $Ra = 10^8$, $1/Ro = 10$, $\Gamma = 1/2$, and (*a*) $Pr = 0.1$, (*b*) $Pr = 0.8$ and (*c*) $Pr = 4.38$.

of the BZF with respect to variations of Pr and Γ by considering time–angle plots of temperature T at $z = H/2$ and $r = R$. Figure 7(*a*) shows that the BZF exists in the flows at different $Pr = 0.1$, 0.8 and 4.38 (also for $Pr = 0.25$, 0.5, 2, 3, 7 and 12.3, not shown), i.e. from small to large Pr. Although there are some quantitative differences among the three cases, they all qualitatively demonstrate the existence of the BZF for more than two decades of Pr.

The qualitative dependence of the BZF on the aspect ratio Γ is shown in figure 8 for three different aspect ratios: $\Gamma = 1/2$, 1 and 2. The BZF is present in all three cases, has the same scaling of BZF width when scaled by H, i.e. δ_0/H is independent of Γ (see figure 9*d* inset), and has a drift period (in units of free-fall time $\tau_{ff} = \sqrt{H/(\alpha g \Delta)} = \tau_\kappa Pr^{-1/2}Ra^{-1/2}$, where $\tau_\kappa = H^2/\kappa$ is the thermal diffusion time) of approximately 70. The quantitative scaling of the drift frequency is analysed later, and the data are tabulated in the Appendix (see table 2). The wavelength λ of the travelling BZF mode is independent of Γ for these three values in a straightforward way, as seen in figure 8, namely $\lambda/H = \pi/2$, so that the number of wavelengths around the circumference is $m = 2\Gamma$ and the wavenumber is $k = 2\pi/\lambda = 4/H$. We note, however, that this relationship is for a limited number of values of Γ and control parameters Ra and Ro. Thus, we make no strong claims to its generality. Indeed, there is already evidence from de Wit *et al.* (2020) that for $\Gamma = 1/5$ one gets $m = 1 \neq 2\Gamma$, and we made additional measurements with $\Gamma = 1/3$ and $3/4$ that also yield $m = 1$. We conjecture that, owing to periodic azimuthal symmetry, m will take on only integer values, similar to the situation for wall mode states (Ecke *et al.* 1992; Goldstein *et al.* 1993; Ning & Ecke 1993; Zhong *et al.* 1993; Liu & Ecke 1999) in cylindrical convection cells. Because of this periodic constraint, one cannot have $m < 1$, so small aspect ratios with $\Gamma \lesssim 1$ have $m = 1$. We also note that the mode-number dependence on Γ of the BZF is similar to that of the Γ dependence of linear wall state mode number, i.e. $m \approx 3\Gamma$ (Goldstein *et al.* 1993; Herrmann & Busse 1993; Kuo & Cross 1993; Ning & Ecke 1993; Liu & Ecke 1999; Zhang & Liao 2009). Given that our states have values of Ra that are 10–100 times greater than the linear wall mode onset Ra_w, this difference is not unreasonable and the correspondence is very suggestive. In particular, a range of mode numbers are stable near onset (Ning & Ecke 1993; Zhong *et al.* 1993; Liu & Ecke 1999) owing to the azimuthally periodic boundary conditions. Significantly above onset there seems to be a selection towards lower mode numbers: for example,
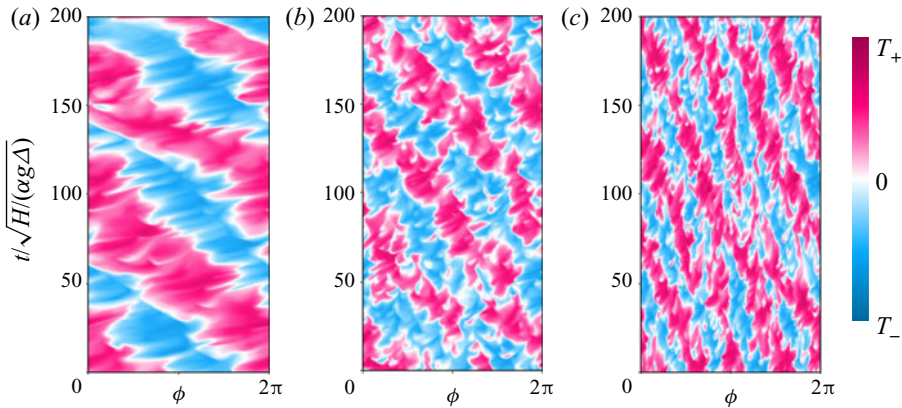
Figure 8. Space–time plots of temperature T at the sidewall, $r = R$, and at half-height, $z = H/2$, for $Ra = 10^8$, $1/Ro = 10$, $Pr = 0.8$, and (*a*) $\Gamma = 1/2$, (*b*) $\Gamma = 1$ and (*c*) $\Gamma = 2$.

Zhong *et al.* (1993, figures 3 and 8) with $\Gamma = 2$ show stable wall modes with $m = 4,\ 5,\ 6$ and 7 near onset but only the $m = 4$ and 5 modes persist for higher Ra, which yields $m = 2\Gamma$ and $m = 2.5\Gamma$, respectively, consistent with our results for the BZF (see also Favier & Knobloch 2020).

3.4. *Spatial and temporal scales*

We next consider the quantitative dependence of the different layer widths on Ra, Ek and Pr, looking for a universal scaling of the form $\delta/H \sim Pr^\xi Ra^\beta Ek^\gamma$. In figure 9(*a*), the dependence of δ_0/H on Ek for $Ra = 10^9$, $Pr = 0.8$ and $2 < 1/Ro < 20$ is shown to be consistent with an $Ek^{2/3}$ scaling, whereas the widths based on other measures scale closely as $Ek^{1/3}$, i.e. γ takes on values of 2/3 and 1/3 for BZF width and velocity layer widths, respectively. (Because the statistical uncertainty in our reported exponents is of the order of 5 %–10 %, we report fractional scalings consistent with the data to within these uncertainties; they are not intended to denote exact results.) As mentioned in Zhang *et al.* (2020), the BZF is characterized by bimodal temperature p.d.f.s near the sidewall. This property was used in both DNS and experimental measurements to identify the BZF over a wide range of Ra. Here, we conduct a more detailed analysis of the DNS data to explore how the width of the BZF changes with Ra. We compute the width at fixed $Ro = Ra^{1/2}Pr^{-1/2}Ek$ so $Ek = Ro\,Ra^{-1/2}Pr^{1/2}$. To determine the scaling with Ra at fixed $Ro = 1/10$, we have that $\delta/H \sim Ra^{\beta-\gamma/2}$. By multiplying by $Ra^{\gamma/2}$ we obtain the scaling exponent β. In figure 9(*b*), we plot $(\delta_0/H)Ra^{1/3}$ and $(\delta/H)Ra^{1/6}$ corresponding to γ values of 2/3 and 1/3, respectively. From this plot, we obtain values for β of 1/4 and 0, respectively. Similarly for the dependence on Pr, we plot in figure 9(*c*) the corrected quantities $(\delta/H)Pr^{\gamma/2}$, which yields δ_0/H scalings for ξ of $-1/4$ for $Pr < 1$ and 0 for $Pr > 1$. The other layer widths based on u_ϕ, u_z and $\mathcal{F}_z$ are independent of Pr for $Pr < 1$ but do not collapse for $Pr > 1$. The separation of the different widths for $Pr > 1$ suggests some interesting behaviour not captured by our scaling ansatz.

Finally, we can collapse all the data for BZF width onto a single scaling curve by plotting in figure 9(*d*) $\delta_0^*/H = \delta_0/H(Pr^{\{1/4,\ 0\}}Ra^{-1/4})$ versus Ek (to compact the different scalings with Pr we denote them as $Pr^{\{1/4,0\}}$ for scaling with $Pr < 1$ and $Pr > 1$, respectively) so that we can conclude that $\delta_0/H \sim Pr^{\{-1/4,0\}}Ra^{1/4}Ek^{2/3}$. The results at one set of
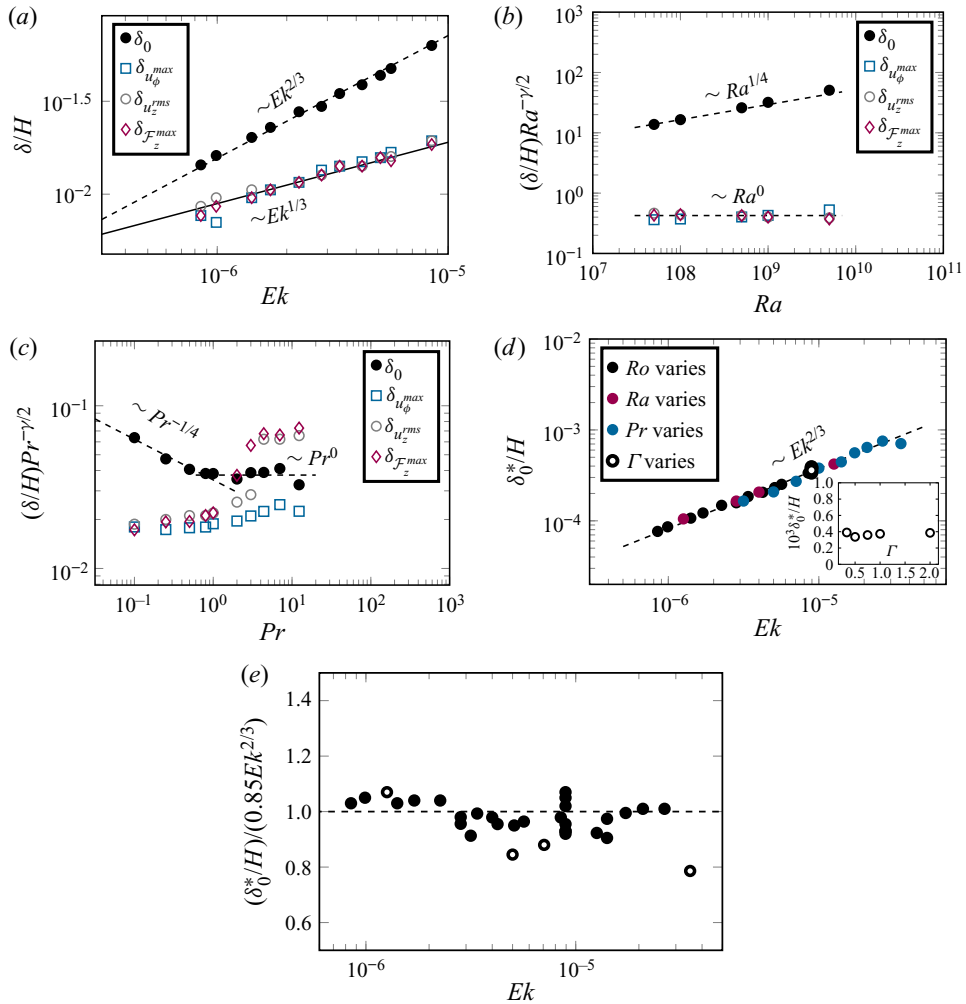
Figure 9. (a) Scaling with *Ek* of characteristic widths $\delta/H \sim Ek^\gamma$ (for δ_0, the distance from the vertical wall to the location where $\langle u_\phi \rangle_t = 0$), for $Ra = 10^9$, $Pr = 0.8$ and $\Gamma = 1/2$. For δ_0/H, one obtains $\gamma \sim 2/3$, whereas for other δ/H, one has $\gamma = 1/3$. (b) Scaling with *Ra* of compensated width $Ra^{\gamma/2}\delta_0/H$ for fixed $1/Ro = 10$ and $Pr = 0.8$. (c) Scaling with *Pr* of compensated width $Pr^{-\gamma/2}\delta_0/H$ for $Ra = 10^8$ and $1/Ro = 10$. (d) Scaling with *Ek* of normalized BZF width $\delta_0^*/H = Ra^{-1/4}Pr^{1/4}\delta_0/H$ (for $Pr < 1$) and $\delta_0^*/H = Ra^{-1/4}Pr^0\delta_0/H$ (for $Pr > 1$); for compactness, we write the two scalings with *Pr* as $Pr^{\{-1/4, 0\}}$. The inset shows δ_0^*/H versus Γ. (e) Compensated plot of BZF width $(\delta_0/H)/(0.85Pr^{\{-1/4, 0\}}Ra^{1/4}Ek^{2/3})$ versus *Ek* (all data from table 2 are shown; open symbols are cases with larger statistical uncertainty owing to shorter averaging time).

parameter values $\{Ra, Pr, Ro\}$ are independent of Γ (see figure 9d inset), which implies that $\delta_0/H \sim \Gamma^0$ (other dependences on Γ are not ruled out for other parameter values, although it is reasonable to assume it to be general in the absence of other data). Thus, we plot in figure 9(d) all the data with different Γ, Pr, Ra and Ek to obtain scalings

$$\delta_0/H \approx 0.85\Gamma^0 Pr^{-1/4}Ra^{1/4}Ek^{2/3}, \quad \text{for } Pr < 1, \tag{3.7}$$

$$\delta_0/H \approx 0.85\Gamma^0 Pr^0 Ra^{1/4}Ek^{2/3}, \quad \text{for } Pr > 1. \tag{3.8}$$

915 A62-12

Figure 10. Scalings of ω_d: (a) data scaled by $Pr^{4/3}Ek^{-5/3}$ showing Ra scaling; (b) data scaled by $Ra^{-1}Ek^{-5/3}$ showing $Pr^{-4/3}$ scaling; and (c) data scaled by $Pr^{4/3}Ra^{-1}$ showing $Ek^{5/3}$ scaling (cases at different Ra (grey squares), at different Pr (red triangles) and at different Ro (blue circles)).

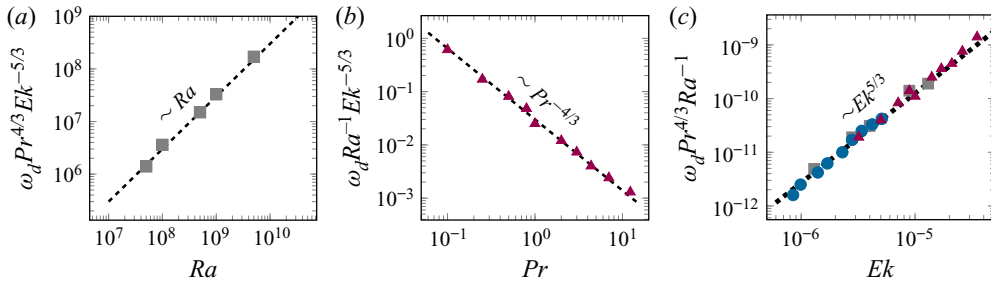We plot in figure 9(e) the scaled BZF width $(\delta_0/H)/(0.85\Gamma^0 Pr^{\{-1/4,\,0\}}Ra^{1/4}Ek^{2/3})$. One sees that the data scatter randomly within $\pm 10\,\%$, quite good agreement.

The BZF drifts anticyclonically, the same as the direction of travelling wall modes of rotating convection (Zhong *et al.* 1991; Ecke *et al.* 1992; Herrmann & Busse 1993; Kuo & Cross 1993). We plot in figure 10(a) the drift frequency $\omega_d \equiv \omega/\Omega$ versus Ra showing scaling as Ra and in figure 10(b) versus Pr showing scaling as $Pr^{-4/3}$(data in both are corrected for constant-Ro conditions). In figure 10(c), we scale out the dependence on Ra and Pr, i.e. $\omega_d Ra^{-1}Pr^{4/3}$, and observe reasonable collapse with $Ek^{5/3}$ scaling. From the cases listed in table 2, we get the frequency scaling in terms of Ra, Pr, Γ and Ek as

$$\omega_d \approx 0.03\,\Gamma^0 Pr^{-4/3} Ra\, Ek^{5/3}. \tag{3.9}$$

The linear dependence on Ra is consistent with earlier results (Horn & Schmid 2017; Favier & Knobloch 2020; de Wit *et al.* 2020) and suggests that there is a correspondence between the states we observe and the nonlinear manifestation of linear wall mode states. The scalings we have determined for ω_d with Ek and Pr will be useful in making a more quantitative comparison with the wall mode hypothesis among datasets with different Ek and Pr. Such an analysis is beyond the scope of the present work and will be presented elsewhere. These scalings, of course, depend on the definition of the time unit. Using the free-fall time or the vertical thermal diffusion time, respectively, we obtain

$$\omega/\sqrt{\alpha g \Delta/H} \approx 0.015\,\Gamma^0 Pr^{-5/6} Ra^{1/2} Ek^{2/3}, \tag{3.10}$$

$$\omega/(\kappa/H^2) \approx 0.015\,\Gamma^0 Pr^{-1/3} Ra\, Ek^{2/3}, \tag{3.11}$$

which both show the same Ek scaling as δ_0, i.e. $Ek^{2/3}$ (see figure 9a). For the three choices of time scale, the drift frequency decreases with increasing Pr for all Pr as opposed to the scaling of δ_0/H, which has different scaling for small and large Pr (see figures 9c and 12b).

As reported in Zhang *et al.* (2020) and shown here in figure 3, the thermal structures drift anticyclonically, opposite to the azimuthal velocity, which is cyclonic near the sidewall, as shown in figure 2(b–d). We show in figure 11(a) that the drift frequency decreases as rotation increases with a scaling $Ek^{2/3}$. In figure 11(b), we show that the near-plate azimuthal velocity u_ϕ^{peak} is also anticyclonic and shows the same scaling behaviour with Ek (see figure 10b) as the BZF width and drift frequency. Based on this observation, we believe that the drift characteristics of the BZF are determined not only by the presence of the vertical wall but also by the near-plate region.

915 A62-13
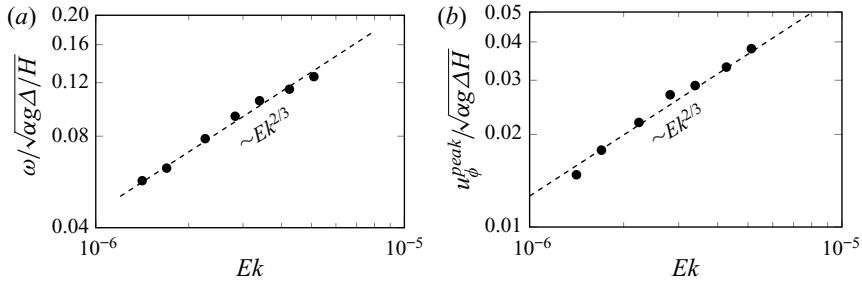
Figure 11. For fixed $Ra = 10^9$ and rotation rates, $1/Ro = 5.6$, 6.7, 8.3, 10, 12.5, 16.7 and 20: (*a*) drift frequency ω of BZF; and (*b*) maximum absolute value of u_ϕ near plates (mean value of two maxima). In both panels $Pr = 0.8$ and $\Gamma = 1/2$.
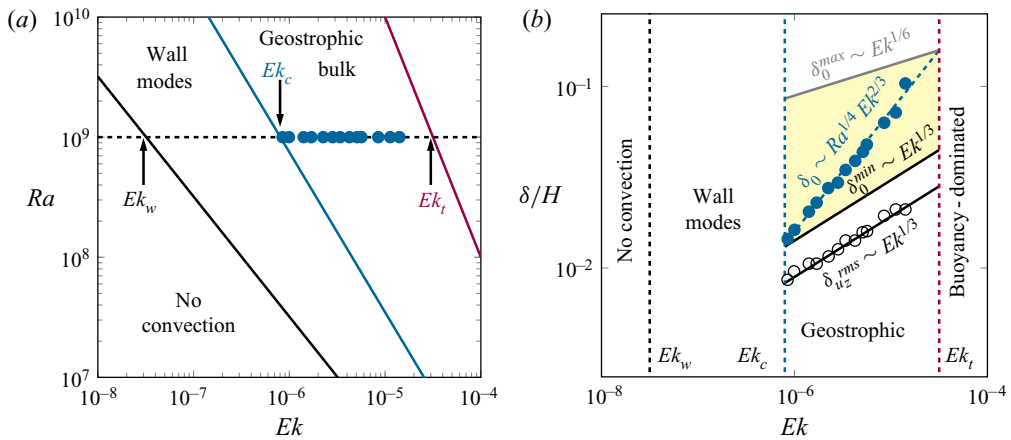
Figure 12. (*a*) The *Ra–Pr* phase diagram. Different rotating convective states are labelled. The dashed horizontal line corresponds to $Ra = 10^9$. Critical *Ek* values Ek_w, Ek_c and Ek_t are indicated. The *Ek* data (solid circles) correspond to values in (*b*). (*b*) Widths of BZF δ_0 and Stewartson $\sim Ek^{1/3}$ layer $\delta_{u_z}^{rms}$ at $Ra = 10^9$ (DNS) versus *Ek*. Vertical dashed lines (black, blue and red, respectively) are the critical Ekman numbers for onset of wall modes (Ek_w), onset of bulk convection (Chandrasekhar 1961; Niiler & Bisshopp 1965) (Ek_c), and transition to rotation-dominated regimes (Ek_t) for $Pr = 0.8$, $Ra = 10^9$ and $\Gamma = 1/2$.

Finally, we consider the range of *Ra* and *Ek* in which the BZF is observed in this study. There are three regions defined by the onset of wall mode convection $Ra_w \approx 32Ek^{-1}$, the onset of bulk convection $Ra_c = AEk^{-4/3}$ and the transition from geostrophic convection (Grooms *et al.* 2010; Julien *et al.* 2012) to buoyancy-dominated convection $Ra_t = Pr Ro_t^2 Ek^{-2}$, where $Ro_t \approx 1$ (see figure 13 in the Appendix) is the transition Rossby number out of the geostrophic regime (Julien *et al.* 1996; King *et al.* 2009; Liu & Ecke 2009; Weiss & Ahlers 2011*b*) as indicated in the *Ra–Ek* phase diagram in figure 12(*a*). Our data fall solely within the geostrophic regime of bulk convection, but we include the other zones for context. According to Chandrasekhar (1961) (see also Clune & Knobloch 1993), the critical Rayleigh number for the onset of convection is $Ra_c \sim Ek^{-4/3}$ with a prefactor *A* that is weakly dependent on *Ek*, in the range 6–8.7 (Chandrasekhar 1961; Niiler & Bisshopp 1965); we use a value of 7.5 consistent with our range of *Ek*.

To illustrate one aspect of this range, we consider the BZF width δ_0/H versus *Ek* for $Ra = 10^9$ in figure 12(*b*). A path of constant $Ra = 10^9$ (figure 12a)

915 A62-14
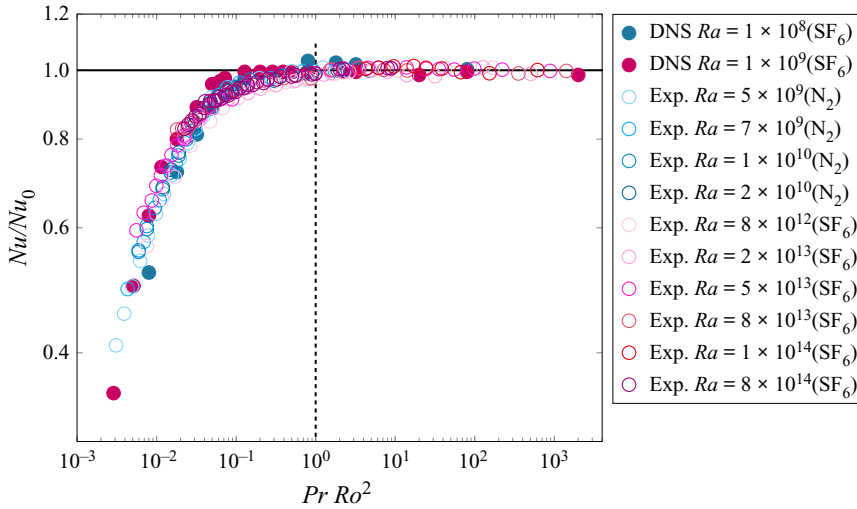
Figure 13. Double-logarithmic scale plot of Nu/Nu_0 versus $PrRo^2$. The horizontal line indicates $Nu/Nu_0 = 1$; the vertical dashed line indicates the value Ro_t, i.e. a transition between buoyancy-dominated convection at larger Ro ($Nu \approx Nu_0$) and the rotation-dominated regime at smaller Ro ($Nu < Nu_0$). Experimental data are from Wedi *et al.* (2021).

yields $Ek_w \approx 32 Ra^{-1} = 3.2 \times 10^{-8}$, $Ek_c = (A\,Ra^{-1})^{3/4} = 8 \times 10^{-7}$ and $Ek_t = Ro_t Pr^{1/2}$ $Ra^{-1/2} = 2.8 \times 10^{-5}$. Here the subscripts 'w', 'c' and 't' correspond, respectively, to the onset of wall mode, bulk convection and transition from rotation to buoyancy-dominated regime. These values are indicated by vertical dashed lines in figure 12(*b*). Knowing the dependence of the critical Ra_c and Ek, and using the relations (3.7) and (3.8), we can evaluate the smallest possible δ_0 for any fixed Ek, i.e. $\delta_0^{min} \sim Ra_c^{1/4} Ek^{2/3} \sim Ek^{1/3}$ (see δ_0^{min} in figure 12*b*). Connecting these onset points, we obtain the black line in the diagram, which is parallel to the Stewartson '1/3' layer scaling. The gap between these two black solid lines depends slightly on A, but the ratio of the BZF width to the Stewartson layer width is constant (based on $\delta_{u_z}^{rms}$) at the onset of convection (the fixed gap). Thus, although the BZF width decreases faster than the Stewartson layer as rotation increases, there is no crossing of the BZF boundary and the boundary of the Stewartson layer at extremely fast rotation because bulk convection ceases before they can cross. Note that all the data considered here fall within the geostrophic range of rotating convection; what happens in the wall mode region is not addressed.

The other bound on the BZF scaling depends on when rotation becomes significant. An estimate is made based on a plot of Nu/Nu_0 versus $Pr\,Ro^2$ for our DNS and for experimental data from Wedi *et al.* (2021) (see figure 13 in the Appendix), where the data for Ra from 10^8 to 10^{14} merge onto a single curve. Here Nu_0 is the Nusselt number in the non-rotating case. Using an empirical estimate $Ro_t \approx 1$ for the onset of the rotation-dominated regimes, i.e. the geostrophic regime, we get an estimate for the largest possible δ_0, for any Ek (grey line in figure 12, that is, $\delta_0^{max} \propto Ra_t^{1/4} Ek^{2/3} \propto Ro_t^{1/2} Ek^{1/6} \approx Ek^{1/6}$). (The value $Pr\,Ro_t^2 \approx 1$ is the onset in figure 13, but in the experiments Pr varies from 0.7 to 0.9 and in the DNS $Pr = 0.8$; thus here we take $Pr = 1$, which gives $Ro_t \approx 1$, for simplicity.)

It is remarkable that the BZF regime is confined by these two critical lines ($\sim Ek^{1/6}$ and $\sim Ek^{1/3}$) and the range confined in between gets broader for higher Ra. In other words, at low Ra, the BZF is only observed over a small range of rotation rates. At large Ra, the BZF exists over a much broader range of rotation rates (Zhang *et al.* 2020; Wedi *et al.* 2021). For any fixed Ra, the BZF exists in a certain Ek range that is determined by the grey and black lines in figure 12(*b*) and the BZF width changes as $\delta_0 \sim Ek^{2/3}$ over that range. How the BZF contributes to the heat transport relative to the contribution of the laterally unbounded system in the geostrophic regime remains an open question. Further, the connection between the BZF and linear wall modes requires additional work to understand the relationship between the two convective states.

4. Conclusion

The BZF is found to be an important flow structure in rapidly rotating turbulent Rayleigh–Bénard convection in the geostrophic regime and is robust over considerable ranges of Ra, Ek, Pr and Γ. The main structure, drift of plume pairs, is found to be a $m = 2\Gamma$ mode for the choices of $\Gamma = 1/2$, 1 and 2; additional values of $\Gamma = 1/3$ and 3/4 yield $m = 1$, suggesting mode 1 for $\Gamma \lesssim 1$. In addition, the BZF carries a large portion of the total heat; its contribution to the total heat transport is approximately 60 % of the heat transport at fast rotation, $Ro < 0.1$, and for $Pr < 1$. For $Pr > 1$, the BZF heat transport contribution drops to approximately 35 %. Understanding this important contribution to the heat transport is essential in analysing experiments in rotating convection in the geostrophic regime.

The scaling of the BZF width δ_0 depends on Pr, Ra and Ek as $\delta_0/H \sim \Gamma^0 Pr^{\{-1/4, 0\}} Ra^{1/4} Ek^{2/3}$ (that is, $Pr^{-1/4}$ for small-to-moderate Pr and independent of Pr for large Pr). The universal scaling of the BZF and the sidewall BLs is very clean for $Pr < 1$ but the BZF is less coherent for $Pr > 1$ and the sidewall BL widths behave differently for those conditions. Further, the sharp decrease in the BZF heat transport contribution similarly marks a transition to a perhaps more complex BZF state for $Pr > 1$. The drift frequency of the BZF shows scaling $\omega/\Omega \sim \Gamma^0 Pr^{-4/3} Ra\, Ek^{5/3}$, indicating that the drift frequency decreases significantly as Pr increases, is proportional to Ra and decreases rapidly with increasing rotation (decreasing Ek). Interestingly, ω seems to be more robust than δ with respect to changes in Pr. Finally, the BZF shares qualitative and some quantitative characteristics with linear wall modes, and establishing the connection between these two states will be an important area of future research.

Declaration of interests. The authors report no conflict of interest.

Author ORCIDs.
- Xuan Zhang https://orcid.org/0000-0001-5684-3064;
- Robert E. Ecke https://orcid.org/0000-0001-7772-5876;
- Olga Shishkina https://orcid.org/0000-0002-6773-6464.

Γ	Pr	Ra	$1/Ro$	t_{avg}/τ_{ff}	N_r	N_ϕ	N_z	$\mathcal{N}_{th}$	$\mathcal{N}_u$	$\mathcal{N}_u^{sw}$	δ_{th}/H	δ_u/H	δ_u^{sw}/H	$\max(h/\eta_k)$
1/2	0.8	5.0×10^7	10	440	90	256	380	43	49	16	3.5×10^{-2}	4.5×10^{-2}	2.3×10^{-2}	0.63
		1.0×10^8	10	500	100	256	380	39	50	17	3.0×10^{-2}	4.9×10^{-2}	2.0×10^{-2}	0.79
		5.0×10^8	10	370	128	320	620	46	89	17	1.6×10^{-2}	5.4×10^{-2}	1.4×10^{-2}	0.67
		1.0×10^9	10	1130	192	512	820	37	101	18	1.2×10^{-2}	5.3×10^{-2}	1.3×10^{-2}	0.85
		5.0×10^9	10	200	256	620	860	39	118	27	7.3×10^{-3}	5.1×10^{-2}	9.4×10^{-3}	1.24
1/2	0.1	1.0×10^8	10	750	256	256	512	70	60	33	7.3×10^{-2}	5.7×10^{-2}	1.2×10^{-2}	1.10
	0.25		10	80	100	256	380	39	50	17	5.1×10^{-2}	5.2×10^{-2}	1.9×10^{-2}	0.77
	0.5		10	250	100	256	380	39	50	17	4.2×10^{-2}	4.9×10^{-2}	1.7×10^{-2}	0.92
	0.8		10	500	100	256	380	39	50	17	3.0×10^{-2}	4.9×10^{-2}	2.0×10^{-2}	0.79
	1		10	450	100	256	380	37	50	17	2.8×10^{-2}	4.8×10^{-2}	2.0×10^{-2}	0.72
	2		10	500	100	256	380	29	53	22	1.8×10^{-2}	5.3×10^{-2}	2.9×10^{-2}	0.80
	3		10	600	100	256	380	26	53	35	1.5×10^{-2}	5.2×10^{-2}	3.4×10^{-2}	0.83
	4.38		10	430	100	256	380	24	50	16	1.3×10^{-2}	4.8×10^{-2}	1.6×10^{-1}	0.86
	7		10	540	100	256	380	24	46	49	1.3×10^{-2}	4.2×10^{-2}	8.9×10^{-2}	0.88
	12.3		10	420	100	256	380	23	41	54	1.2×10^{-2}	3.3×10^{-2}	1.0×10^{-1}	0.88
1/3	0.8	1.0×10^8	10	810	96	256	320	28	34	22	2.8×10^{-2}	3.8×10^{-1}	2.0×10^{-2}	0.59
1/2			10	500	100	256	380	39	50	17	3.0×10^{-2}	4.8×10^{-2}	2.0×10^{-2}	0.79
3/4			10	830	128	256	380	38	53	17	3.4×10^{-2}	5.8×10^{-1}	2.0×10^{-2}	0.91
1			10	1480	180	320	320	22	36	15	3.5×10^{-2}	6.5×10^{-2}	2.0×10^{-2}	0.90
2			10	1500	256	320	320	25	46	14	4.0×10^{-2}	9.0×10^{-2}	2.1×10^{-2}	1.24

Table 2. For caption see next page.

Boundary zonal flows in rotating turbulent convection

X. Zhang, R. E. Ecke and O. Shishkina

Γ	Pr	Ra	$1/Ro$	t_{avg}/τ_{ff}	N_r	N_ϕ	N_z	$\mathcal{N}_{th}$	$\mathcal{N}_u$	$\mathcal{N}_u^{sw}$	δ_{th}/H	δ_u/H	δ_u^{sw}/H	$\max(h/\eta_k)$
1/2	0.8	1.0×10^9	0.5	965	192	512	768	14	78	42	7.8×10^{-3}	5.6×10^{-2}	3.4×10^{-2}	0.94
			2	1020	192	512	768	14	87	28	7.8×10^{-3}	6.5×10^{-2}	2.1×10^{-2}	0.94
			2.5	1410	192	512	768	14	88	28	7.7×10^{-3}	6.6×10^{-2}	2.1×10^{-2}	0.94
			3.3	1400	192	512	768	15	90	26	8.0×10^{-3}	6.8×10^{-2}	2.0×10^{-2}	0.94
			5	1630	192	512	768	16	88	22	8.8×10^{-3}	6.5×10^{-2}	1.6×10^{-2}	0.92
			5.6	480	180	280	680	34	105	25	9.0×10^{-3}	6.5×10^{-2}	1.6×10^{-2}	1.13
			6.7	480	180	280	680	35	102	23	9.8×10^{-3}	6.3×10^{-2}	1.4×10^{-2}	1.10
			8.3	500	180	280	680	38	99	23	1.1×10^{-2}	5.8×10^{-2}	1.4×10^{-2}	1.07
			10	1130	192	512	820	37	101	18	1.2×10^{-2}	5.3×10^{-2}	1.3×10^{-2}	0.85
			12.5	400	128	320	620	45	83	15	1.5×10^{-2}	4.8×10^{-2}	1.2×10^{-2}	1.20
			16.7	400	128	320	620	54	73	13	2.1×10^{-2}	3.8×10^{-2}	1.1×10^{-2}	1.10
			20	400	128	320	620	63	65	12	2.8×10^{-2}	3.0×10^{-2}	9.5×10^{-3}	1.03
			28.6	40	128	320	620	83	49	12	4.8×10^{-2}	1.8×10^{-2}	9.5×10^{-3}	0.90
			33.3	37	128	320	620	86	48	11	5.0×10^{-2}	1.7×10^{-2}	8.5×10^{-3}	0.89

Table 2 (cntd). Details of the DNS: including the time of statistical averaging, t_{avg}, normalized with the free-fall time τ_{ff}; the number of nodes N_r, N_ϕ and N_z in the directions r, ϕ and z, respectively; the numbers of nodes within the thermal BL $\mathcal{N}_{th}$ (near the plates), within the viscous BL $\mathcal{N}_u$ (near the plates), and within the viscous BL $\mathcal{N}_u^{sw}$ (near the sidewall); the relative thicknesses of the viscous BL δ_u/H and the thermal BL near the plates δ_{th}/H, and the viscous BL near the sidewall δ_u^{sw}/H; and the maximal value of the ratio of the mesh size to the mean Kolmogorov microscale, $\max(h/\eta_k)$.

Γ	Pr	Ra	Ek	$1/Ro$	ω_κ	ω_{ff}	ω_d	ω_d^*
1/2	0.8	5.0×10^7	1.3×10^{-5}	10	6.3×10^1	1.0×10^{-2}	1.3×10^{-2}	1.9×10^{-10}
		1.0×10^8	8.9×10^{-6}	10	1.3×10^2	1.5×10^{-2}	1.8×10^{-2}	1.4×10^{-10}
		5.0×10^8	4.0×10^{-6}	10	3.3×10^2	1.7×10^{-2}	2.1×10^{-2}	3.1×10^{-11}
		1.0×10^9	2.8×10^{-6}	10	5.7×10^2	2.0×10^{-2}	2.5×10^{-2}	1.9×10^{-11}
		5.0×10^9	1.3×10^{-6}	10	1.7×10^3	2.6×10^{-2}	3.3×10^{-2}	4.9×10^{-12}
1/2	0.1	1.0×10^8	3.2×10^{-6}	10	1.1×10^2	3.3×10^{-2}	4.2×10^{-2}	1.9×10^{-11}
	0.25		5.0×10^{-6}	10	1.0×10^2	2.0×10^{-2}	2.5×10^{-2}	4.0×10^{-11}
	0.5		7.1×10^{-6}	10	1.2×10^2	1.7×10^{-2}	2.1×10^{-2}	8.3×10^{-11}
	0.8		8.9×10^{-5}	10	1.3×10^2	1.5×10^{-2}	1.8×10^{-2}	1.4×10^{-10}
	1.0		1.0×10^{-5}	10	9.1×10^1	9.1×10^{-3}	1.1×10^{-2}	1.1×10^{-10}
	2.0		1.4×10^{-5}	10	1.1×10^2	8.0×10^{-3}	1.0×10^{-2}	2.5×10^{-10}
	3.0		1.7×10^{-5}	10	1.2×10^2	6.7×10^{-3}	8.4×10^{-3}	3.6×10^{-10}
	4.38		2.1×10^{-5}	10	1.0×10^2	5.0×10^{-3}	6.3×10^{-3}	4.5×10^{-10}
	7.0		2.6×10^{-5}	10	1.2×10^2	4.5×10^{-3}	5.7×10^{-3}	7.6×10^{-10}
	12.3		3.5×10^{-5}	10	1.4×10^2	4.0×10^{-3}	5.0×10^{-3}	1.4×10^{-9}
1/2	0.8	1.0×10^8	8.9×10^{-6}	10	1.3×10^2	1.5×10^{-2}	1.8×10^{-2}	1.4×10^{-10}
1				10	1.4×10^2	1.6×10^{-2}	2.0×10^{-2}	1.5×10^{-10}
2				10	1.4×10^2	1.6×10^{-2}	2.0×10^{-2}	1.5×10^{-10}
1/2	0.8	1.0×10^9	5.1×10^{-6}	5.6	7.1×10^2	2.5×10^{-2}	5.7×10^{-2}	4.2×10^{-11}
			4.2×10^{-6}	6.7	6.6×10^2	2.3×10^{-2}	4.4×10^{-2}	3.3×10^{-11}
			3.4×10^{-6}	8.3	6.3×10^2	2.2×10^{-2}	3.4×10^{-2}	2.5×10^{-11}
			2.8×10^{-6}	10	5.7×10^2	2.0×10^{-2}	2.5×10^{-2}	1.9×10^{-11}
			2.3×10^{-6}	12.5	3.8×10^2	1.3×10^{-2}	1.3×10^{-2}	1.0×10^{-11}
			1.7×10^{-6}	16.7	3.1×10^2	1.1×10^{-2}	8.4×10^{-3}	6.2×10^{-12}
			1.4×10^{-6}	20	2.6×10^2	9.1×10^{-3}	5.7×10^{-3}	4.2×10^{-12}
			9.9×10^{-7}	28.6	2.2×10^2	7.7×10^{-3}	3.4×10^{-3}	2.5×10^{-13}
			8.5×10^{-7}	33.3	1.7×10^2	5.9×10^{-3}	2.2×10^{-3}	1.6×10^{-13}

Table 3. Values of Γ, Ra, Pr, Ek, Ro^{-1}, $\omega_\kappa = \omega H^2/\kappa$, $\omega_{ff} = \omega(H/(g\alpha\Delta))^{1/2}$, $\omega_d = \omega/\Omega$ and $\omega_d^* = \omega_d Pr^{4/3} Ra^{-1}$. (For $\Gamma = 1/3$ and 3/4, there are insufficient data to determine ω.)

Appendix

We tabulate here a full characterization of the parameters in the DNS (see table 2) and compare our results for *Nu* with experimental data from Wedi *et al.* (2021). The excellent agreement is a strong indication that our DNS are fully resolved. We also include the resulting numerical values of the BZF drift frequency for different choices of time scale (see table 3), namely ω_κ, ω_{ff} and ω_d for different parameter values Γ, Pr, Ra, Ek and $1/Ro$.

REFERENCES

AHLERS, G., GROSSMANN, S. & LOHSE, D. 2009 Heat transfer and large scale dynamics in turbulent Rayleigh–Bénard convection. *Rev. Mod. Phys.* **81**, 503–537.

AURNOU, J.M., BERTIN, V., GRANNAN, A.M., HORN, S. & VOGT, T. 2018 Rotating thermal convection in liquid gallium: multi-modal flow, absent steady columns. *J. Fluid Mech.* **846**, 846–876.

BODENSCHATZ, E., PESCH, W. & AHLERS, G. 2000 Recent developments in Rayleigh–Bénard convection. *Annu. Rev. Fluid Mech.* **32**, 709–778.

BOUBNOV, B.M. & GOLITSYN, G.S. 1986 Experimental study of convective structures in rotating fluids. *J. Fluid Mech.* **167**, 503–531.

BOUBNOV, B.M. & GOLITSYN, G.S. 1990 Temperature and velocity field regimes of convective motions in a rotating plane fluid layer. *J. Fluid Mech.* **219**, 215–239.

BUELL, J.C. & CATTON, I. 1983 The effect of wall conduction on the stability of a fluid in a right circular cylinder heated from below. *Trans. ASME: J. Heat Transfer* **105**, 255–260.

CHANDRASEKHAR, S. 1961 *Hydrodynamic and Hydromagnetic Stability*. Clarendon.

CHENG, J.S., MADONIA, M., GUZMÁN, A.J.A. & KUNNEN, R.P.J. 2020 Laboratory exploration of heat transfer regimes in rapidly rotating turbulent convection. *Phys. Rev. Fluids* **5**, 113501.

CLUNE, T. & KNOBLOCH, E. 1993 Pattern selection in rotating convection with experimental boundary conditions. *Phys. Rev. E* **47**, 2536–2550.

ECKE, R.E. & NIEMELA, J.J. 2014 Heat transport in the geostrophic regime of rotating Rayleigh–Bénard convection. *Phys. Rev. Lett.* **113**, 114301.

ECKE, R., ZHONG, F. & KNOBLOCH, E. 1992 Hopf bifurcation with broken reflection symmetry in rotating Rayleigh–Bénard convection. *Europhys. Lett.* **19** (3), 177–182.

FAVIER, B. & KNOBLOCH, E. 2020 Robust wall states in rapidly rotating Rayleigh–Bénard convection. *J. Fluid Mech.* **895**, R1.

GOLDSTEIN, H.F., KNOBLOCH, E., MERCADER, I. & NET, M. 1993 Convection in a rotating cylinder. Part 1 Linear theory for moderate Prandtl numbers. *J. Fluid Mech.* **248**, 583–604.

GOLDSTEIN, H.F., KNOBLOCH, E., MERCADER, I. & NET, M. 1994 Convection in a rotating cylinder. Part 2. Linear theory for low Prandtl numbers. *J. Fluid Mech.* **262**, 293–324.

GROOMS, I., JULIEN, K., WEISS, J.B. & KNOBLOCH, E. 2010 Model of convective Taylor columns in rotating Rayleigh–Bénard convection. *Phys. Rev. Lett.* **104** (22), 224501.

HART, J.E., KITTELMAN, S. & OHLSEN, D.R. 2002 Mean flow precession and temperature probability density functions in turbulent rotating convection. *Phys. Fluids* **14**, 955.

HERRMANN, J. & BUSSE, F.H. 1993 Asymptotic theory of wall-attached convection in a rotating fluid layer. *J. Fluid Mech.* **255**, 183–194.

HORN, S. & SCHMID, P.J. 2017 Prograde, retrograde, and oscillatory modes in rotating Rayleigh–Bénard convection. *J. Fluid Mech.* **831**, 182–211.

HORN, S. & SHISHKINA, O. 2014 Rotating non-Oberbeck–Boussinesq Rayleigh–Bénard convection in water. *Phys. Fluids* **26**, 055111.

HORN, S. & SHISHKINA, O. 2015 Toroidal and poloidal energy in rotating Rayleigh–Bénard convection. *J. Fluid Mech.* **762**, 232–255.

JULIEN, K., KNOBLOCH, E., RUBIO, A.M. & VASIL, G.M. 2012 Heat transport in low-Rossby-number Rayleigh–Bénard convection. *Phys. Rev. Lett.* **109**, 254503.

JULIEN, K., LEGG, S., MCWILLIAMS, J. & WERNE, J. 1996 Rapidly rotating turbulent Rayleigh–Bénard convection. *J. Fluid Mech.* **322**, 243–273.

KING, E.M., STELLMACH, S., NOIR, J., HANSEN, U. & AURNOU, J.M. 2009 Boundary layer control of rotating convection systems. *Nature* **457**, 301–304.

KOOIJ, G.L., BOTCHEV, M.A., FREDERIX, E.M.A., GEURTS, B.J., HORN, S., LOHSE, D., VAN DER POEL, E.P., SHISHKINA, O., STEVENS, R.J.A.M. & VERZICCO, R. 2018 Comparison of computational codes for direct numerical simulations of turbulent Rayleigh–Bénard convection. *Comput. Fluids* **166**, 1–8.

KUNNEN, R.P.J., CLERCX, H.J.H., GEURTS, B.J., VAN BOKHOVEN, L.J.A., AKKERMANS, R.A.D. & VERZICCO, R. 2008 Numerical and experimental investigation of structure-function scaling in turbulent Rayleigh–Bénard convection. *Phys. Rev. E* **77**, 016302.

KUNNEN, R.P.J., STEVENS, R.J.A.M., OVERKAMP, J., SUN, C., VAN HEIJST, G.F. & CLERCX, H.J.H. 2011 The role of Stewartson and Ekman layers in turbulent rotating Rayleigh–Bénard convection. *J. Fluid Mech.* **688**, 422–442.

KUO, E.Y. & CROSS, M.C. 1993 Traveling-wave wall states in rotating Rayleigh–Bénard convection. *Phys. Rev. E* **47**, R2245–R2248.

LIU, Y. & ECKE, R. 1999 Nonlinear traveling waves in rotating Rayleigh–Bénard convection: stability boundaries and phase diffusion. *Phys. Rev. E* **59**, 4091–4105.

LIU, Y. & ECKE, R.E. 1997 Transport scaling in turbulent Rayleigh–Bénard convection: effects of rotation and Prandtl number. *Phys. Rev. Lett.* **79**, 2257.

LIU, Y. & ECKE, R.E. 2009 Heat transport measurements in turbulent Rayleigh–Bénard convection. *Phys. Rev. E* **80**, 036314.

LOHSE, D. & XIA, K.-Q. 2010 Small-scale properties of turbulent Rayleigh–Bénard convection. *Annu. Rev. Fluid Mech.* **42**, 335–364.

LUCAS, P.G.J., PFOTENHAUER, J.M. & DONNELLY, R.J. 1983 Stability and heat transfer of rotating cryogens. Part 1. influence of rotation on the onset of convection in liquid ^{4}He. *J. Fluid Mech.* **129**, 251–264.

NAKAGAWA, Y. & FRENZEN, P. 1955 A theoretical and experimental study of cellular convection in rotating fluids. *Tellus* **7**, 1–21.

NIILER, P.P. & BISSHOPP, F.E. 1965 On the influence of Coriolis force on onset of thermal convection. *J. Fluid Mech.* **22** (4), 753–761.

NING, L. & ECKE, R. 1993 Rotating Rayleigh–Bénard convection: aspect-ratio dependence of the initial bifurcations. *Phys. Rev.* E **47**, 3326–3333.

PFOTENHAUER, J.M., NIEMELA, J.J. & DONNELLY, R.J. 1987 Stability and heat transfer of rotating cryogens. Part 3. Effects of finite cylindrical geometry and rotation on the onset of convection. *J. Fluid Mech.* **175**, 85–96.

ROSSBY, T.H. 1969 A study of Bénard convection with and without rotation. *J. Fluid Mech.* **36**, 309–335.

SAKAI, S. 1997 The horizontal scale of rotating convection in the geostrophic regime. *J. Fluid Mech.* **333**, 85–95.

SÁNCHEZ-ÁLVAREZ, J.J., SERRE, E., DEL ARCO, E.C. & BUSSE, F.H. 2005 Square patterns in rotating Rayleigh–Bénard convection. *Phys. Rev.* E **72**, 036307.

SHISHKINA, O., HORN, S., WAGNER, S. & CHING, E.S.C. 2015 Thermal boundary layer equation for turbulent Rayleigh–Bénard convection. *Phys. Rev. Lett.* **114**, 114302.

SHISHKINA, O., STEVENS, R.J.A.M., GROSSMANN, S. & LOHSE, D. 2010 Boundary layer structure in turbulent thermal convection and its consequences for the required numerical resolution. *New J. Phys.* **12**, 075022.

SHISHKINA, O., WAGNER, S. & HORN, S. 2014 Influence of the angle between the wind and the isothermal surfaces on the boundary layer structures in turbulent thermal convection. *Phys. Rev.* E **89**, 033014.

STELLMACH, S., LISCHPER, M., JULIEN, K., VASIL, G., CHENG, J.S., RIBEIRO, A., KING, E.M. & AURNOU, J.M. 2014 Approaching the asymptotic regime of rapidly rotating convection: boundary layers versus interior dynamics. *Phys. Rev. Lett.* **113**, 254501.

STEVENS, R.J.A.M., VERZICCO, R. & LOHSE, D. 2010 Radial boundary layer structure and Nusselt number in turbulent Rayleigh–Bénard convection. *J. Fluid Mech.* **643**, 495–507.

VOROBIEFF, P. & ECKE, R.E. 2002 Turbulent rotating convection: an experimental study. *J. Fluid Mech.* **458**, 191–218.

WEDI, M., VAN GILS, D., BODENSCHATZ, E. & WEISS, S. 2021 Rotating turbulent thermal convection at very large Rayleigh numbers. *J. Fluid Mech.* **912**, A30.

WEISS, S. & AHLERS, G. 2011*a* Heat transport by turbulent rotating Rayleigh–Bénard convection and its dependence on the aspect ratio. *J. Fluid Mech.* **684**, 407–426.

WEISS, S. & AHLERS, G. 2011*b* The large-scale flow structure in turbulent rotating Rayleigh–Bénard convection. *J. Fluid Mech.* **688**, 461–492.

DE WIT, X.M., GUZMAN, A.J.A., MADONIA, M., CHENG, J.S., CLERCX, H.J. & KUNNEN, R.P. 2020 Turbulent rotating convection confined in a slender cylinder: the sidewall circulation. *Phys. Rev. Fluids* **5**, 023502.

ZHANG, X., VAN GILS, D.P.M., HORN, S., WEDI, M., ZWIRNER, L., AHLERS, G., ECKE, R.E., WEISS, S., BODENSCHATZ, E. & SHISHKINA, O. 2020 Boundary zonal flow in rotating turbulent Rayleigh–Bénard convection. *Phys. Rev. Lett.* **124**, 084505.

ZHANG, K. & LIAO, X. 2009 The onset of convection in rotating circular cylinders with experimental boundary conditions. *J. Fluid Mech.* **622**, 63–73.

ZHONG, F., ECKE, R. & STEINBERG, V. 1991 Asymmetric modes and the transition to vortex structures in rotating Rayleigh–Bénard convection. *Phys. Rev. Lett.* **67**, 2473–2476.

ZHONG, F., ECKE, R. & STEINBERG, V. 1993 Rotating Rayleigh–Bénard convection: Asymmetric modes and vortex states. *J. Fluid Mech.* **249**, 135–159.

ZHONG, J.-Q., STEVENS, R.J.A.M., CLERCX, H.J.H., VERZICCO, R., LOHSE, D. & AHLERS, G. 2009 Prandtl-, Rayleigh-, and Rossby-number dependence of heat transport in turbulent rotating Rayleigh–Bénard convection. *Phys. Rev. Lett.* **102**, 044502.

ZWIRNER, L., KHALILOV, R., KOLESNICHENKO, I., MAMYKIN, A., MANDRYKIN, S., PAVLINOV, A., SHESTAKOV, A., TEIMURAZOV, A., FRICK, P. & SHISHKINA, O. 2020 The influence of the cell inclination on the heat transport and large-scale circulation in liquid metal convection. *J. Fluid Mech.* **884**, A18.